

Proton intensity spectra during the solar energetic particle events of May 17, 2012 and January 6, 2014

P. Kuhl¹, S. Banjac¹, N. Dresing¹, R. Gómez-Herrero², B. Heber¹,
A. Klassen¹, and C. Terasa¹

¹ Institute for experimental and applied physics, University Kiel, 24118 Kiel, Germany
e-mail: kuehl@physik.uni-kiel.de

² Space Research Group, University of Alcalá, 28871 Alcalá de Henares, Spain

Received 28 August 2014 / Accepted 18 March 2015

ABSTRACT

Context. Ground-level enhancements (GLEs) are solar energetic particle events that show a significant intensity increase at energies that can be measured by neutron monitors. The most recent GLE-like events were recorded on May 17, 2012 and January 6, 2014. They were also measured by sophisticated instrumentation in space such as PAMELA and the Electron Proton Helium INstrument (EPHIN) onboard SOHO. Since neutron monitors are only sensitive to protons above 400 MeV with maximum sensitivity at 1 to 2 GeV, the spectra of such weak GLE-like events (January 6, 2014) can only be measured by space instrumentation.

Aims. We show that the SOHO/EPHIN is capable of measuring the solar energetic particle proton event spectra between 100 MeV and above 800 MeV.

Methods. We performed a GEANT Monte Carlo simulation to determine the energy response function of EPHIN. Based on this calculation, we derived the corresponding proton energy spectra. The method was successfully validated against previous PAMELA measurements.

Results. We present event spectra from EPHIN for May 17, 2012 and January 6, 2014. During the event in May 2012, protons were accelerated to energies above 700 MeV, while we found no significant increase for protons above 600 MeV during the event on January 6, 2014.

Key words. instrumentation: detectors – Sun: flares – Sun: coronal mass ejections (CMEs) – solar-terrestrial relations – space vehicles: instruments

1. Introduction

Forbush (1946) reported the first solar energetic particle (SEP) event that is now called a ground-level enhancement (GLE). These events are produced when ions with energies above several hundred of MeVs create a nuclear cascade in the Earth atmosphere. As a consequence, detectors at ground level measure an increase above the galactic cosmic-ray background (GCRB). Since then, 71 GLEs have been reported that exceed the GCRB by barely a few percent. The largest measured increase of about 4500% above the GCRB was observed during GLE 5 on February 23, 1956 (Reames 2013). During solar cycle 24, only the event on May 17, 2012 was unambiguously measured by more than one neutron monitor. In addition to understanding the physics of GLEs, that is, the acceleration process, the recent paper by Thakur et al. (2014) claimed that the event on January 6, 2014 was GLE 72 and sparked a discussion on the definition of a GLE (Usoskin, priv. comm., see also www.nmdb.eu). The question of the definition whether a solar energetic particle event is recorded as a GLE or not depends on several factors; the measurement capabilities at ground level for magnetic and atmospheric cutoff rigidities, for instance, need to be lower than one GV. To overcome this situation, it would be better to rely on spacecraft measurements outside the Earth magnetosphere. Here we show that the Kiel Electron Proton Helium Instrument (EPHIN, Müller-Mellin et al. 1995) onboard the SOHO spacecraft

can indeed provide such energy spectra for selected particle events.

On May 17, 2012 at 01:25 UT, the NOAA active region 11476, located at N11W76, produced a class M5.1 flare (Gopalswamy et al. 2013; Shen et al. 2013). Around 01:50 UT, the worldwide network of neutron monitors¹ detected the first ground-level enhancement in solar cycle 24. The energy spectra as measured by the payload for antimatter-matter exploration and light-nuclei astrophysics (PAMELA; Picozza et al. 2007) have been reported by Bazilevskaya et al. (2013), indicating that protons with energies of up to one GeV and helium of up to 100 MeV/nucleon were accelerated during that event.

On January 6, 2014 STEREO A and B detected a flare in the extreme ultraviolet (EUV) at 7:30 UT with a double maximum at 7:55 UT and 8:15 UT that occurred 25 degree behind the western limb as seen from Earth. The event was associated with a coronal mass ejection (CME) and an EUV wave. Type II and III radio bursts were recorded by measurements on ground as well as in space. Eleven one-minute running-mean averages exceed the pre-event distribution at the South Pole neutron monitor and the bare counter at about 8:10 UT, which agrees well with the GOES observations (Thakur et al. 2014). Note that Thakur et al. (2014) report an onset time of 7:58 UT, indicating the uncertainty of different methods to determine the event onset. Since we did not

¹ <http://www.nmdb.eu/>

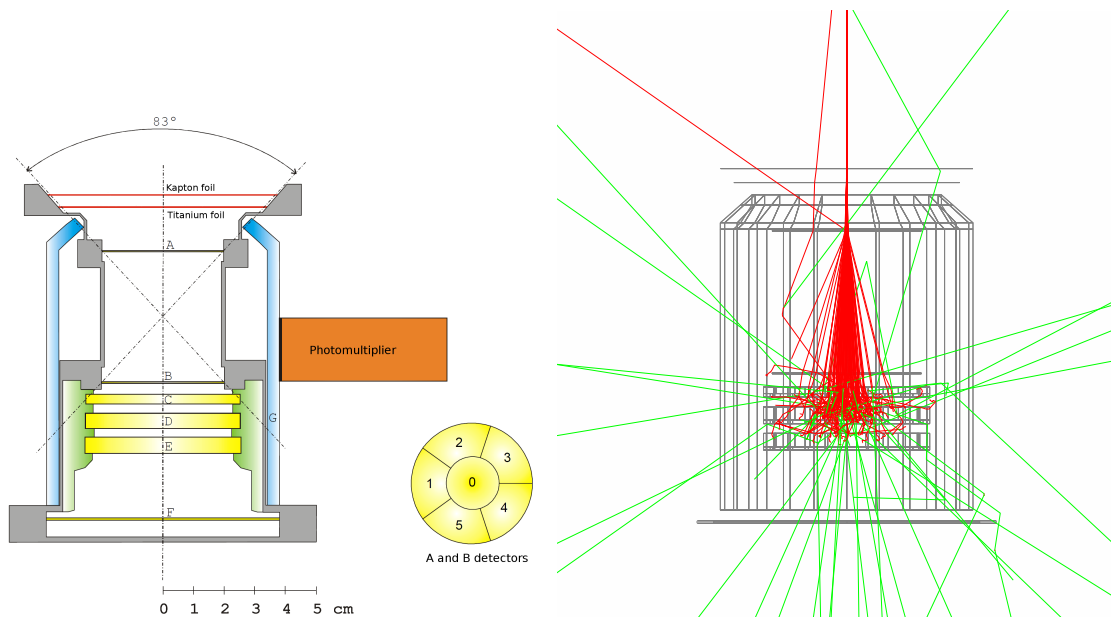


Fig. 1. *Left:* sketch of the EPHIN instrument. *Right:* instrument as modeled in the GEANT4 simulations including a beam of 100 electrons (5 MeV, red) as well as gamma secondaries (green). Note that the detailed housing shown in the left sketch is also included in the GEANT4 model. It is not shown here for greater clarity.

find any statistically significant intensity increase (above 4σ) for other neutron monitors such as Tixie Bay or McMurdo, it is an open question whether this event can be defined as ground-level enhancement number 72. To make significant progress here, it is essential to know the particle, that is, the proton energy spectra above the atmosphere. In this paper, we present a new method for extending the measurements capabilities of SOHO/EPHIN into the energy range from ~ 100 MeV to above 800 MeV for protons.

2. GEANT 4 simulation of the Electron Proton Helium Instrument

The Electron Proton Helium INstrument (EPHIN, Müller-Mellin et al. 1995) is part of the Comprehensive Suprathermal and Energetic Particle Analyzer (COSTEP) instrument suite on-board the Solar and Heliospheric Observatory (SOHO). SOHO was launched in December 1995 and has an orbit around the Lagrangian point L1. Figure 1 (left) shows a sketch of the instrument, which consists of six solid-state detectors (labeled A–F) enclosed in a scintillator that acts as anticoincidence (G). The measurements of EPHIN rely on the $dE/dx-E$ method, which yields count rates for different ranges in the silicon detector stack. As described by Müller-Mellin et al. (1995), different ions and even isotopes can be identified based on the energy deposition in the first detector ΔE_A and the sum of the energy depositions E in all detectors. In addition to the total counts of these different coincidence conditions, energy losses in each detector are available for a statistical sample of individual particle tracks, allowing a detailed analysis of the measured particles including the calculation of energy spectra for electrons up to ≈ 10 MeV and ions up to ≈ 50 MeV/nucleon.

In addition, the instrument allows measuring penetrating particles that are combined in an integral channel. It is more challenging to calculate the energy for these particles because the total energy of the particle and the particle type are a priori unknown. Furthermore, the coincidence condition for penetrating particles can also be fulfilled by particles entering the instrument

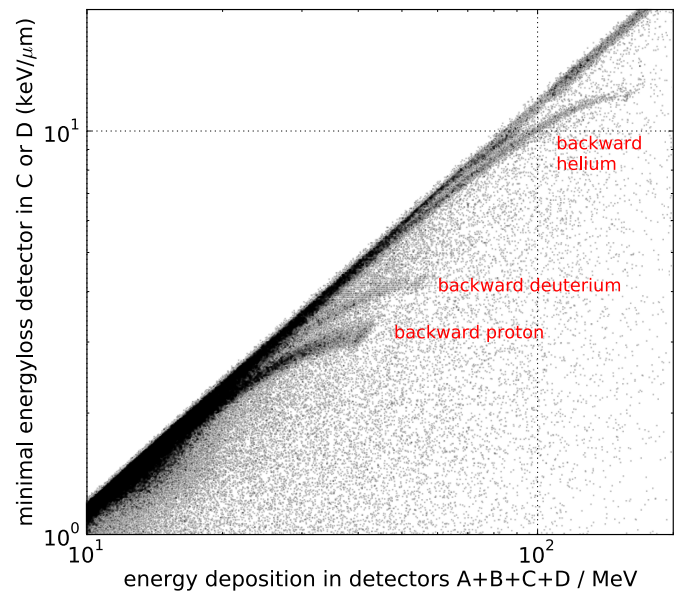


Fig. 2. Minimum of the energy loss in detectors C and D as a function of the total energy loss seen in the instrument in December 2009. The expected tracks for backward-penetrating particles (protons, deuterium, and helium) are marked. For details see text.

from behind. However, the statistical sample of energy losses does include penetrating particles. Based on these data, Fig. 2 displays the minimum energy loss per path length in detectors C and D (i.e., $\min(dE_c/b_c, dE_d/b_d)$ with dE_x energy loss in detector x and b_x the thickness of the detector) as a function of the total energy loss seen in the detector stack for the Galactic cosmic-ray background (data from December 2009). The tracks for backward-penetrating protons, deuterium, and helium have been identified and marked based on the Bethe-Bloch equation. These tracks merge with the tracks of forward-penetrating particles along the diagonal, and thus a separation between forward and backward penetrating particles is only possible in a limited

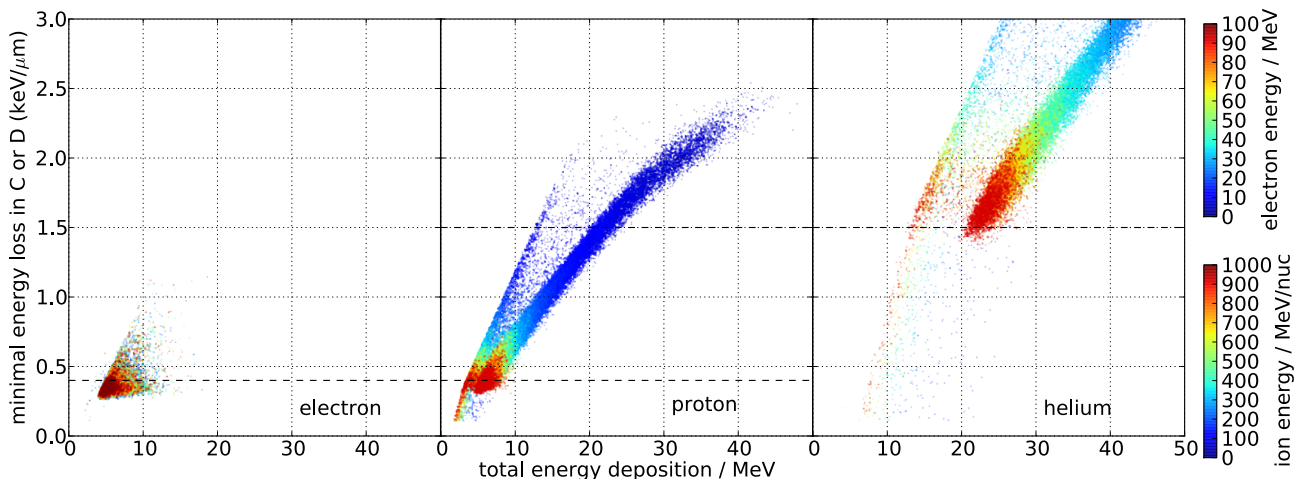


Fig. 3. Simulation results of the energy losses for electrons, protons, and helium particles. Note the different color scales for electrons and ions. For a colored version of the plot, we refer to the online version of this article.

energy range. Furthermore, backward-penetrating particles have to pass the spacecraft, which acts as an additional shielding, and thus the energy threshold of forward- and backward-penetrating particles differs substantially.

To address these problems, a GEANT4 Monte Carlo simulation that considers various processes such as electromagnetic and hadronic interaction of particles in matter and the production of secondary particles has been set up (GEANT4 Collaboration 2006, version 4.9.6.2). Different calculations for forward- and backward-penetrating particles were performed separately. Figure 1 (right) displays the instrument as it is implemented in the GEANT4 simulation (see also Böhm et al. 2007) with typical particle tracks calculated in the simulation. Shown are results for 5 MeV electrons (red trajectories) that scatter in the detector stack and produce secondary gamma rays (green). Since our focus is on solar energetic particle events that may be considered to be a GLE but are only recorded at neutron monitors with cut off rigidities below 2 GV, energies above 1 GeV per nucleon for ions and 100 MeV for electrons are not considered because it is unlikely that they are accelerated in these events. The assumed upper limit chosen for protons was confirmed for the event in May 2012 by Bazilevskaya et al. (2013), and since the event in January 2014 was observed by fewer neutron monitors with the lowest rigidity cutoff, its highest energy can be considered to be even lower. The upper limit for electrons is based on observations by Moses et al. (1989). The lowest energy that was simulated is defined by the necessary energy of a particle to penetrate the entire instrument (Müller-Mellin et al. 1995). Thus, we chose energies ranging from 50 MeV/nucleon to 1 GeV/nucleon for ions and from 10 MeV up to 100 MeV for electrons. Since no detailed information regarding the real mass distribution of the s/c is available, the shielding was estimated to be equivalent to 10 cm of aluminum based on spacecraft mass and geometry. Below we discuss the modeling results for forward- and backward-penetrating particles separately. This is realized by two simulations featuring a half-sphere located in front of and behind the instrument. Particles are then emitted equally distributed in angles over the half-sphere.

2.1. Forward-penetrating particles

Here we describe the results of the GEANT4 simulations using particles that incite the detector stack from the front. To cover the

energy space with the same probability, the intensity was chosen to be constant over energy. A year after the launch of SOHO, one of the detectors, detector E, started to become noisy, therefore it was decided to remove the detector from the coincidence logic as described in Müller-Mellin et al. (1995). Figure 3 shows from left to right the minimum of the energy depositions per path length of detectors C and D versus the total energy registered in the instrument for electrons, protons, and helium particles. The color of each dot represents the particle energy in the simulation as indicated by the color bars on the right. The minimum of the energy loss per path length of detectors C or D was used to reduce the influence of scattering. In the figure, two different particle tracks can be identified for the ions. The main population with higher total energy deposition is based on particles that deposit energy in every detector A–F, while the second track is caused by particles that pass through the detectors A–D and F, without energy deposition in detector E. From Fig. 1 it is obvious that only a small fraction of penetrating trajectories can miss detector E without hitting the anticoincidence. Furthermore, Fig. 3 indicates that the measured energy in detectors C and D is not affected by these trajectories because the energy losses in C and D at a given energy (color-coded in the figure) are the same for both tracks. Therefore we used the minimum of the energy loss per path length in C or D throughout instead of the total energy deposition E .

From Fig. 3 it is evident that there are overlaps of the proton signatures with both the electron and the helium signatures above or below the dashed lines, respectively. Since an independent particle identification is not possible, the proton spectra are contaminated by electrons and helium at low and high energies. In the intermediate region with energy depositions between 0.4 keV/μm and 1.5 keV/μm such contaminations are unlikely.

To explore the energy range that corresponds to that energy depositions, histograms of the energy deposition for different particles are presented in Fig. 4. The proton energies of 100 MeV and 800 MeV are chosen such that the mean of the energy loss distributions is clearly contained in the limits of 0.4 keV/μm and 1.5 keV/μm. Because the electron energy only slightly affects the energy depositions (see Fig. 3), the energy was chosen arbitrarily as 20 MeV. For the helium particles, an energy of 1 GeV per nucleon was selected because these high energies result in the smallest energy depositions per path length. The figure shows that energy depositions between 0.4 keV/μm and 1.5 keV/μm are mainly caused by protons in the energy range between 100 MeV

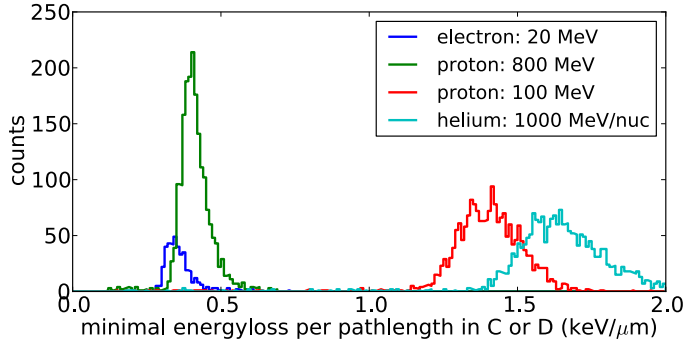


Fig. 4. Histogram of the energy deposition for electrons, protons, and helium particles based on mono-energetic simulations.

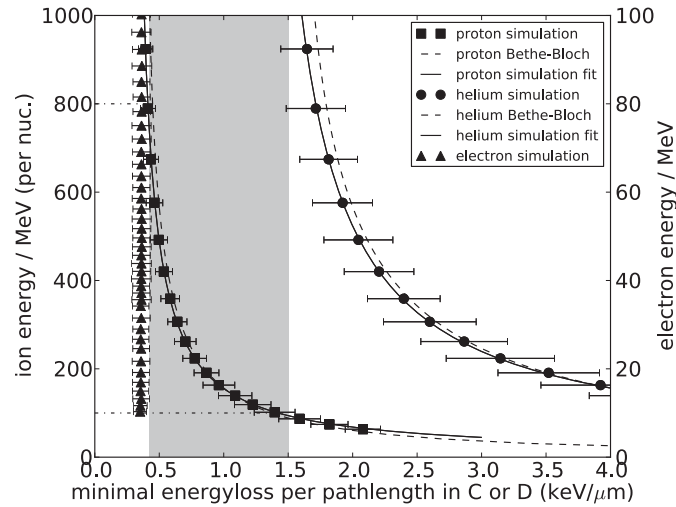


Fig. 5. Simulated kinetic energy of the particles as function of the resulting energy deposition in the detector. Simulation results for forward-penetrating electrons (triangle, right axes), protons (squares), and helium particles (circles) are shown. In addition, calculations based on the Bethe-Bloch equation (dashed lines) and fit results (solid lines) for the ions are presented. The shaded area marks energy losses that are most probably caused by protons.

and 800 MeV. Since lower and higher energy depositions can only be caused by electrons or helium particles, respectively, the derived proton spectrum based on the method described in this work is limited to these energies.

Furthermore, the energy loss distributions for all particles tend to have a Gaussian shape, and hence the mean value and the standard deviation of the distributions can be used to facilitate the analysis further. Because we are interested in reconstructing the total energy of a particle based on the energy deposition, the simulated energy is shown as a function of the resulting energy deposition in Fig. 5. The figure shows in agreement with Fig. 4 that the main contribution of energy depositions between $0.4 \text{ keV}/\mu\text{m} \lesssim \frac{dE}{dx} \lesssim 1.5 \text{ keV}/\mu\text{m}$ (marked by the shaded area) is made by protons with energies between $100 \text{ MeV} \lesssim E \lesssim 800 \text{ MeV}$ (indicated by dashed-dotted lines).

To calculate the total energy of the measured particles based on the energy depositions, inversion methods have often been used in the past (compare Böhm et al. 2007). Before applying such sophisticated mathematical methods, we start with a simple procedure based on the results above. Our approach is supported by the fact that the response function in the energy range of interest does not depend on energy (black curve in Fig. 6) and an analytic relation between energy deposition and total energy

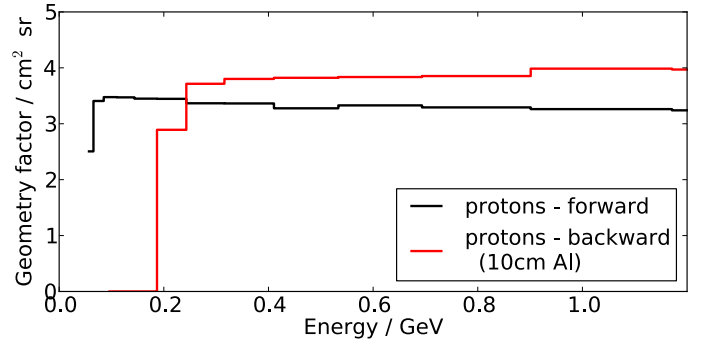


Fig. 6. Geometry factors for forward- and backward- (10 cm aluminum shielding) penetrating protons.

can be expressed by a fit, as presented in Fig. 5. The function reads

$$E = a + b/(dE - c), \quad (1)$$

where E is the kinetic energy of the measured particle (in MeV per nuc.), dE (in MeV) corresponds to the energy deposition in the detector elements and a , b , c are variables. This function is motivated by the Bethe-Bloch equation with parameters a and c added to take relativistic corrections into account. Fitting this function to the simulation results for protons as shown in Fig. 5 defines the parameter to

$$a = 4.65 \pm 1.06,$$

$$b = 1.09 \times 10^{-1} \pm 8.81 \times 10^{-4} \text{ and}$$

$$c = 2.74 \times 10^{-4} \pm 1.05 \times 10^{-6}.$$

With this function, the total energy of penetrating protons in the given energy range can be derived. Based on the measured energy loss data, this results in a histogram of the total energy that can be converted into a spectrum exploiting the instrument geometry factor and considering the ratio of the total counts to the size of the statistical sample.

2.2. Backward-penetrating particles

A GEANT4 simulation as presented above was also performed for backward-penetrating particles by including an approximated shielding by the spacecrafts body of 10 cm aluminum behind the instrument. Particles were injected from a half-sphere behind the aluminum layer.

Figure 7 presents the simulation results for backward-penetrating particles. Similar to the forward-penetrating particles, two particle tracks can be identified for ions as some of them may miss detector E (see Fig. 3). For electrons, the shape of the energy-loss distribution does not change, and therefore, like forward-penetrating electrons, they do not contaminate the energy-loss histogram in the considered ranges.

For the ions, however, differences between forward and backward results occur. Regarding the total energy of the particles, energy loss is caused by backward-penetrating particles with higher energy than the energy loss caused by forward-penetrating particles. This effect can be explained by the fact that particles coming from behind the instrument have to penetrate the shielding and therefore will reach the instrument with only a fraction of their initial energy. The calculated geometry factors shown in Fig. 6 for backward- and forward-penetrating protons support this explanation. While protons need to have a kinetic

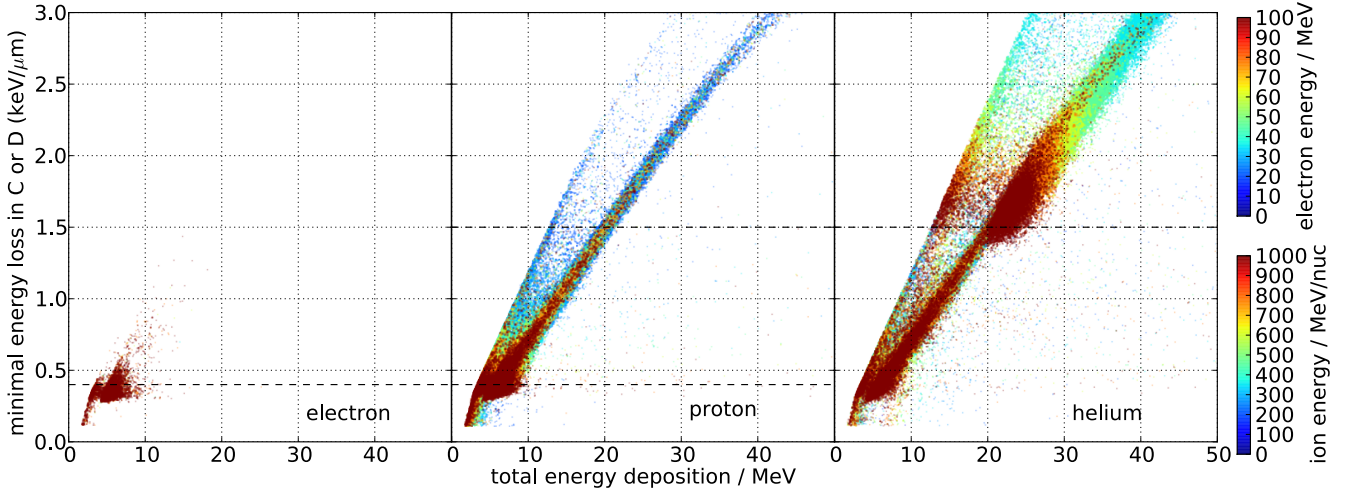


Fig. 7. Simulation results of the energy losses for backward-penetrating electrons, protons, and helium particles with 10 cm of aluminum shielding. Note the different color scales for electrons and ions. For a colored version of the plot, we refer to the online version of this article.

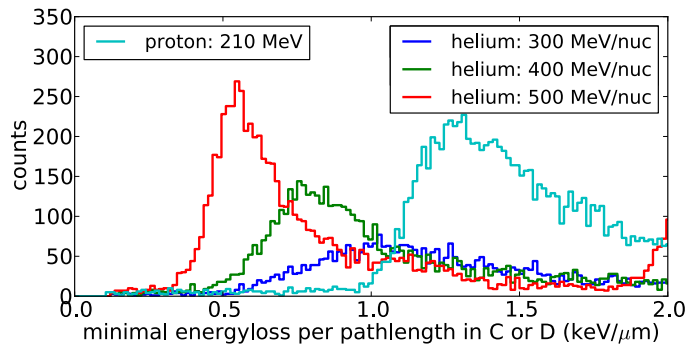


Fig. 8. Histograms of the energy deposition for backward-penetrating helium particles and protons with different energies. Above 300 MeV per nucleon, a population of secondary protons is clearly visible.

energy of ≈ 50 MeV to trigger the integral channel when coming from the front of the detector, backward-penetrating protons need to have at least ≈ 200 MeV to do so. This effect is confirmed by the energy loss histogram of 200 MeV backward-penetrating protons presented in Fig. 8: the distribution shows similar energy losses as for the 50 MeV forward-penetrating protons (Fig. 4). Furthermore, backward-penetrating ions can cause higher energy depositions in detectors C and D than forward-penetrating ions. This is because detectors A and B have a different material thickness ($450 \mu\text{m}$) than detectors E and F ($5500 \mu\text{m}$).

The results for helium do not only differ in terms of their total energy as a result of the shielding effect, but also in the distribution of energy losses in general. In contrast to the forward-penetrating helium, backward-penetrating helium can cause energy losses below the threshold, indicated by the dashed line, in a significant amount. The histograms of the energy deposition presented in Fig. 8 indicate that in addition to the expected high energy losses, a second distribution at typical energy losses of protons is caused by these backward-penetrating helium particles. The contamination of these secondaries starts to rise above energies of 300 MeV per nucleon of the primary helium particle. According to the simulation, these energy depositions are secondary protons created by helium particles in the shielding that then enter the instrument.

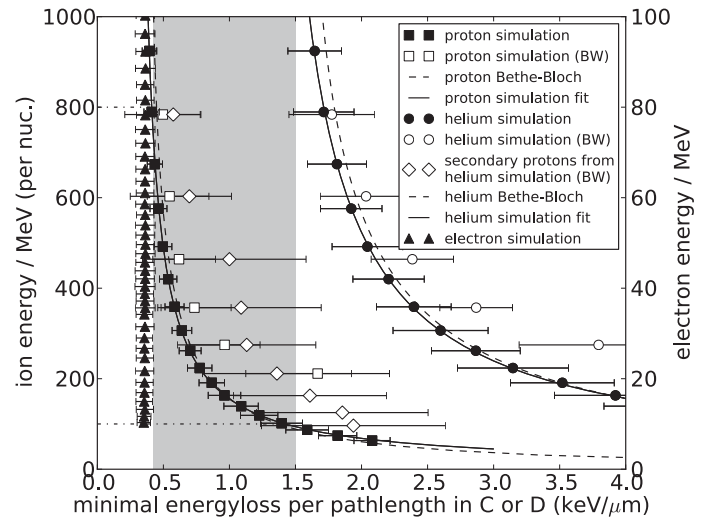


Fig. 9. Simulated kinetic energy of the particles as a function of the resulting energy deposition in the detector. Energy deposition in the detector based on the kinetic energy of the particle. Simulation results for forward- (filled) and backward- (open) penetrating electrons (triangle, right axes), protons (squares), helium particles (circles), and secondary protons (diamonds) are shown. In addition, calculations based on the Bethe-Bloch equation (dashed lines) and fit results (solid lines) for the ions are presented. The shaded area marks energy losses that are most probably caused by protons.

2.3. Combined signals and error estimations

In Fig. 9 the results from the backward simulations are summed as open symbols in addition to the results of the forward-penetrating simulations (filled symbols). Note that secondary protons created by primary helium distributions are presented individually. The figure indicates that backward-penetrating protons mimic forward-penetrating protons with lower energies, resulting in errors in the spectrum calculated by the method described above. However, as solar events are known to have soft spectra whose intensity quickly decreases with increasing energy (Mewaldt et al. 2012), low-energy protons are more likely than particles with higher energies that mimic them. To illustrate this point, Fig. 10 shows the energy-loss histograms for forward- and backward-penetrating protons resulting from

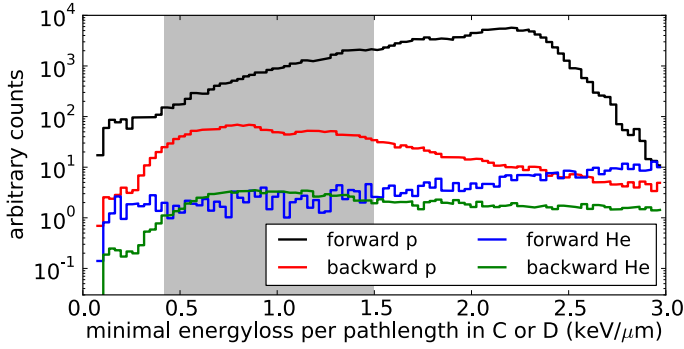


Fig. 10. Energy-loss histogram with $\gamma = -3$ for forward- and backward-penetrating protons and helium particles with a helium-to-proton ratio of 10%.

simulations based on a power-law spectrum $I(E) = I_0 \cdot \left(\frac{E}{E_0}\right)^{-\gamma}$ with a spectral index of $\gamma = 3$ as typically observed during solar events (excluding the time during the onset of the events, see [Mewaldt et al. 2012](#)). The range of energy losses taken into account for the spectrum calculated is marked by shading. The figure shows that under the considered circumstances the highest contribution of backward-penetrating protons occurs at low dE/dx and is in the order of 20%. At higher energy losses, the contribution is substantially lower (down to 2%) because of the shielding of the spacecraft.

In addition to the proton results, Fig. 10 presents energy-loss histograms for forward- and backward-penetrating helium (including the produced secondary protons) with similar spectral shape and an assumed flux ratio $He/p = 10\%$. This flux ratio is a reasonable worst-case scenario based on ERNE measurements ([Torsti et al. 1995](#)), which we examined for the time periods of the events². From the figure, it is obvious that the influence of helium particles is negligible as these particles only account for $\approx 1\%$ of the total counts, while up to $\approx 20\%$ of the counts are caused by backward-penetrating protons.

Based on this analysis, we conclude that the maximum systematic error of the intensity can be approximated to be 20%. Furthermore, the majority of the counts during time-periods with steep spectra are caused by forward-penetrating particles. Hence, we apply the geometry factor for forward penetrating protons as displayed in Fig. 6 for the spectrum calculations in the following sections.

3. Application to SEP events

In this section we apply the described procedure to two events observed on May 17, 2012 (GLE 71) and January 6, 2014. To validate our method, the spectrum for the GLE 71 is compared to PAMELA results.

3.1. Event on May 17, 2012

On May 17, 2012 at 01:25 UT, the NOAA active region 11476, located at N11W76, produced a class M5.1 flare. Around 01:50 UT, the worldwide network of neutron monitors³ detected the first ground-level enhancement in solar cycle 24. Relativistic electrons measured by EPHIN started to rise at 1:51 UT and triggered the Relativistic Electron Alert System for Exploration

² Data accessible at <http://www.srl.utu.fi/projects/erne/erne.html>

³ <http://www.nmdb.eu/>

([Posner et al. 2009](#)). The event was detected by a few neutron monitor stations, with the strongest signal detected at the South Pole. Count rates of the Neutron Monitors Apatity and South Pole and the EPHIN intensity measured by the integral channel, 25–50 MeV protons and relativistic electrons, are displayed in Fig. 11 left. While the duration of the event as recorded by the neutron monitors is a few hours, the intensity time profile of the EPHIN measurements remained above background for several days. As a result of SOHO commanding, no data were available after 7:00 UT.

Remote-sensing observations from the terrestrial point of view and from STEREO have been extensively discussed by [Gopalswamy et al. \(2013\)](#) and [Shen et al. \(2013\)](#). [Gopalswamy et al. \(2013\)](#) noted that the M5.1 flare started, peaked, and ended at 01:25, 01:47, and 02:14 UT, respectively. A metric type II radio burst was reported at 01:32 UT. The coronagraphs on STEREO A and on SOHO first observed the CME at 01:40 UT and 01:48 UT. The event onset time for near relativistic protons was between $1:43 \text{ UT} < t_{\text{On}} < 2:00 \text{ UT}$ (see also [Papaioannou et al. 2014](#)). The energy spectra as measured by PAMELA ([Picozza et al. 2007](#)) have been reported by [Bazilevskaya et al. \(2013\)](#) and indicate that protons with energies of up to 900 MeV and helium of up to 100 MeV/nucleon have been measured by PAMELA.

Figure 11 right shows the pre-event GCR background (May, 16: 00–24:00 UT, black diamonds) and the event spectra for the GLE71 on May 17, 2012 (03:00–05:00 UT, red squares) measured by SOHO/EPHIN as calculated by the method described in Sect. 2. While the background spectrum shows artifacts, the background-subtracted event spectrum does not show any instrumental features. The artifacts in the background spectrum below $\approx 100 \text{ MeV}$ correspond to energy losses $\geq 1.5 \text{ keV}/\mu\text{m}$, which are caused by high-energy helium particles. In the event spectrum, this contamination disappears because of the spectral shape and the low helium-to-proton ratio (compare Sect. 2.2).

To compare them with the EPHIN intensities, the values provided by [Bazilevskaya et al. \(2013\)](#) for the time period 03:39–03:49 UT are also shown in Fig. 11 right (blue circles). Note that our method is applied to a longer timeseries than the PAMELA spectrum because the temporal resolution of our method is limited for statistical reasons. While the intensities agree perfectly at energies above 300 MeV, they differ by less than two sigma at lower energies. It is important to note that the spectral slope as well as the overall magnitude agree reasonably well, and therefore, regarding the simplicity of our method compared with the complex instrumentation, the results are promising. Therefore, we also applied the method to the event on January 6, 2014.

3.2. Event on January 6, 2014

The SEP event on January 6, 2014 was associated with a flare that occurred 25 degrees behind the western limb at coordinates S15W115, a broad CME with angular width ≥ 200 degrees, and a large EUV wave.

The EUV flare and the dome-shaped EUV-wave ([Warmuth 2007](#)) were clearly observed by both STEREO spacecraft and the SDO. The spacecraft constellation as well as the magnetic connectivity to the flare location is displayed in Fig. 12. The flare starts at 07:30 UT, showing a double maximum at 07:55 and 08:15 UT, and was accompanied by a coronal and IP type II radio burst as observed by CALLISTO and IZMIRAN (onset at 07:43 UT at $\geq 400 \text{ MHz}$), and SWAVES, respectively. The flare-associated type III radio bursts occur simultaneously with and

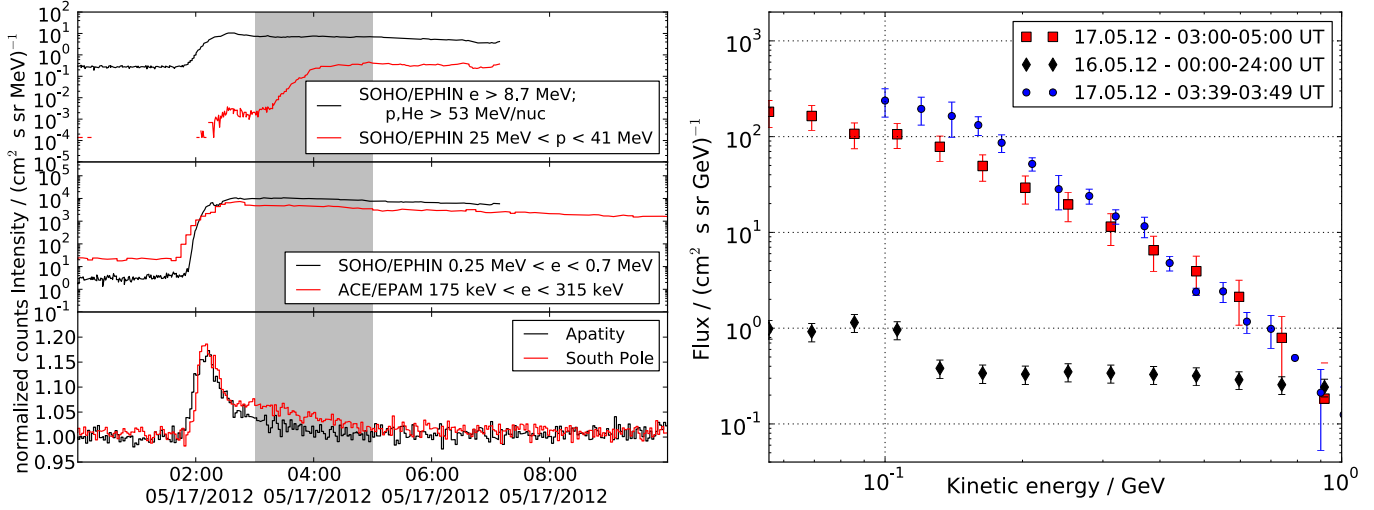


Fig. 11. *Left:* time profile of the GLE in May 2012. We present the integral channel and protons measured by SOHO/EPHIN (*top*), electrons measured by SOHO/EPHIN and ACE/EPAM (*middle*), and neutron monitor count rates. *Right:* calculated GCR background (black diamonds) and background-subtracted event spectrum (red squares). The PAMELA spectrum supplied by [Bazilevskaya et al. \(2013\)](#) is shown for comparison (blue circles).

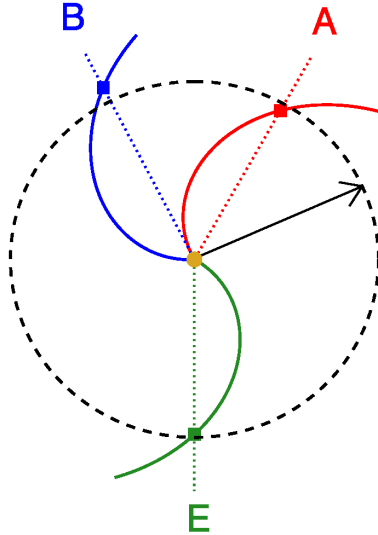


Fig. 12. Location of the flare (indicated by the arrow) with respect to the spacecraft constellation. The flare location was determined from the STEREO A image.

during the coronal/IP type II burst and were detected only at SWAVES at ≤ 16 MHz, suggesting that the type III generating electrons were accelerated and/or injected into the IP space by the propagating shock. Therefore it is plausible to assume that the type II/III bursts onset around 07:43 UT is the injection time of SEPs into IP space. The broad CME is discussed by [Thakur et al. \(2014\)](#). The associated in situ IP shock was detected at STA at 17:05 UT on January 8, but no in situ signatures were detected at STEREO B or at SOHO and ACE.

Figure 13 left displays the particle intensity time-profiles during the time period from 6 UT to 16 UT. In the lower panel, five-minute averages of the count rate of the South Pole neutron monitor are shown. The intensity of these particles remains above the Galactic cosmic-ray background from ~ 8 to $\sim 10:45$ UT, and the maximum intensity increase is $\sim 2\%$. In comparison to the neutron monitor, the middle panel displays the intensity time-profiles of near relativistic electron as measured by SOHO/EPHIN and ACE/EPAM. The energy range of EPHIN

and EPAM are 250 to 700 keV and 175 to 315 keV, respectively. The speed of these electrons is similar to that of the protons that caused the increase in the neutron monitor count rates. From the ACE measurements we found an onset time at 8:10 UT. Unfortunately, SOHO/EPHIN has a data gap during the event onset, with the first data available at 8:43 UT. The upper panel displays the time profile of the integral channel (black curve) and of 25 to 50 MeV protons (red curve). Marked by shading is the time from the beginning of data transmission at 8:43 to 10:45 UT, that is, the time period the neutron monitor count rates are higher than the GCR background.

The proton event spectrum is displayed in Fig. 13 right together with a background spectrum that was calculated for January 3, 2014. The GCR background spectrum again shows the contamination of relativistic helium at lower proton energies followed by a flat spectrum that is expected from the contribution of forward- and backward-penetrating protons. The event spectrum is characterized by a power-law-like distribution, with an increase of about two orders of magnitude below 100 MeV and a factor of 5 at 500 MeV with respect to the pre-event background. Above 500 MeV, the intensity values show a trend to be higher than the background, but the values are statistically limited. We were able to compare the GLE 71 spectrum with PAMELA measurements, but no proton spectra for this event are available to us. Thus it is important to discuss the potential influence of different components on our results. Relativistic helium is one of the components that may alter the result. If we assume as a worst case 10% for the helium-to-proton ratio, the calculated proton spectra above 700 MeV rule out a major contribution of helium. Electrons may alter the proton spectrum at higher energies. Since the contribution of electrons to the proton spectrum shows no strong energy dependence, a flattening of the calculated spectrum above 500 MeV is expected (see Fig. 9). Assuming a power law for the proton spectrum, the contribution of backward-penetrating particles should flatten the spectrum. However, as discussed above, the contribution of all these additional components is expected to be minor for solar energetic particle events (see Fig. 10).

From the flattening of the spectrum above 600 MeV, we conclude this spectral roll-over energy to be the highest energy to which particles are accelerated in the event. This finding is

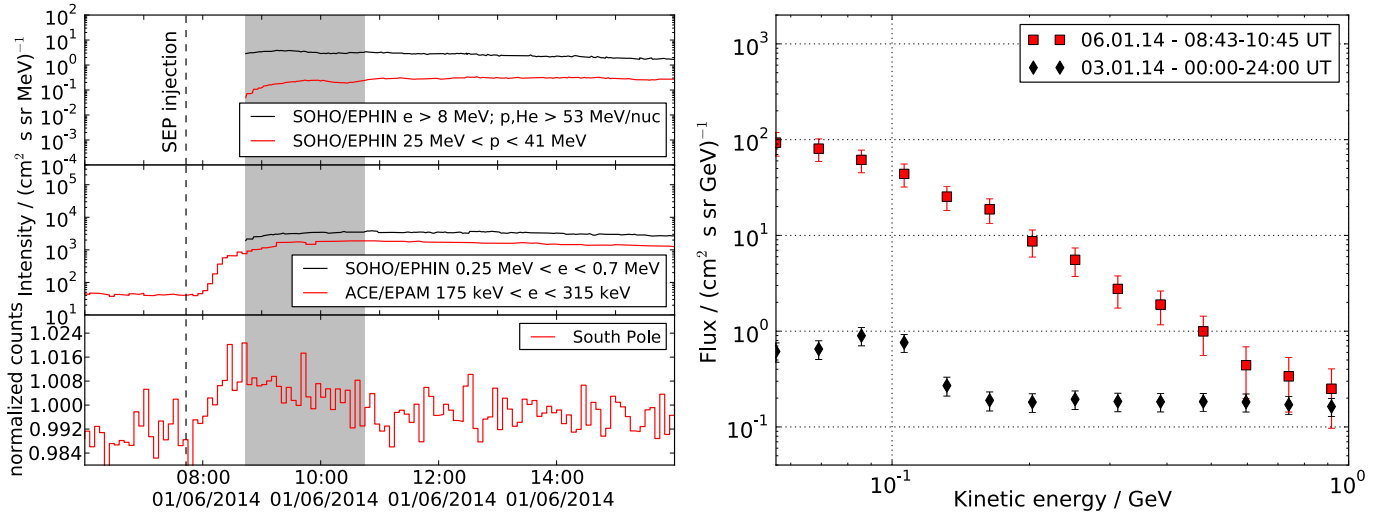


Fig. 13. *Left:* time profile of the event on January 6, 2014. We present the integral channel and protons measured by SOHO/EPHIN (*top*), electrons measured by SOHO/EPHIN and ACE/EPAM (*middle*), and neutron monitor count rates. The dashed lines indicates the injection time of SEPs into IP space (07:43 UT). *Right:* calculated GCR background (black diamonds) and background-subtracted event spectrum (red squares).

supported by the fact that no statistically significant increase above the background is observed above this energy (i.e., the higher energy bins of the event and the background spectrum agree when the error bars are taken into account). This finding is supported by GOES measurements, which only show a weaker increase in intensity above 700 MeV compared to significant increases between 400 and 700 MeV (see Fig. 1a in Thakur et al. 2014).

4. Summary and discussion

Ground-level enhancements are solar energetic particle events that show a significant intensity increase at energies that can be measured by ground-based instrumentation, that is, by neutron monitors. The solar energetic particle event on January 6, 2014, which was measured by the South Pole neutron monitors, has opened the discussion in the community of how a GLE is defined⁴. In contrast to previous GLEs with significant count rate increases at several locations, there is no possibility to determine the energy spectra from ground-based measurements for the event on January 6, 2014 (e.g., Matthiä et al. 2009). Since the energy required to penetrate both the magnetosphere and the atmosphere of Earth varies from a few hundred MeV to several GeV based on the cutoff rigidity (i.e., latitudinal and longitudinal position as well as atmospheric pressure), there is an increasing need to derive proton energy spectra from spacecraft measurements in this energy range. Knowledge of the interplanetary energy spectrum of solar events is especially important for investigating particle transport in the magnetosphere and atmosphere as well as for the neutron monitor and the space weather community.

We showed that SOHO/EPHIN is well-suited to provide these proton spectra for the events on May 17, 2012 and January 6, 2014. Although the instrument was designed to measure stopping particles only, that is, protons up to 50 MeV, the telescope provides sufficient information for particles such as protons above 50 MeV that penetrate the instrument to extend the energy range. Using a GEANT 4 simulation, we determined the response function of electrons, protons, and helium for energies from 5 MeV to 100 MeV and from 50 MeV/nucleon to

1 GeV/nucleon for forward- and backward-penetrating particles. As a promising result, the simulation for forward-penetrating particles shows that protons can be unambiguously identified in the energy range from about 100 MeV to below 800 MeV. The calculations for particles (protons, helium, and electrons) penetrating the instrument from behind give a significant background and overlap in the energy range of interest. A clear example for these contributions are the cosmic-ray background spectra displayed in Figs. 11 and 13 with a prominent helium contribution below 120 MeV and a flat spectrum for higher energies due to the combination of forward and backward penetrating protons. The latter are in part produced by hadronic interactions of helium particles in the spacecraft material. To determine quiet-time GCR spectra, more detailed investigations are needed. Fortunately, long averaged spectra of solar energetic particle events tend to follow a power law or a Band function (Tylka et al. 2006; Band et al. 1993) with a spectral index γ above 3 (e.g., Tylka et al. 2006). The simulation indicates that the contribution of the backward-penetrating protons is lower than 20% for such steep spectra and is therefore lower than the contribution of the forward-penetrating protons. Since the response function for protons above 50 MeV is nearly constant (see Fig. 6), we derived a simplified inversion method from measured energy losses to kinetic energy and intensity.

The procedure was successfully applied to the GLE on May 17, 2012 and was validated against the PAMELA measurements. To shed some light on the discussion about the SEP on January 6, 2014, we also applied our method to this event. The resulting background-subtracted spectrum is shown in Fig. 14 in comparison to the background-subtracted spectrum for May 17, 2012. The ratio of the two spectra is also displayed in the figure. During the 2012 event, the intensities at 100 and 600 MeV are two and four times higher than during the 2014 event, indicating that the later spectrum steepens faster than that in May 2012. This softer spectrum results in a lower maximum energy, which is important for detecting a SEP event by ground-based instrumentation. From South Pole measurements there is no doubt that the event was recorded by ground-based measurements at an air pressure of 690 mBar and vertical cutoff rigidities below 1 GV (corresponding to 500 MeV for protons). If South Pole were the only location of a cosmic-ray detector at ground, such as

⁴ See Thakur et al. (2014) and <http://nest2.nmdb.eu>

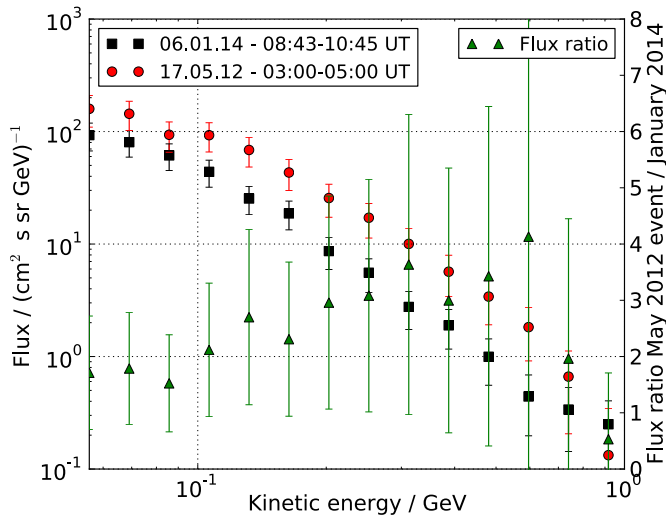


Fig. 14. Background-subtracted spectra for the events in May 2012 (red circles) and January 2014 (black squares) (see Figs. 11 and 13). The ratio of the two events is presented on the right-hand axis (green triangles).

MSL/RAD on Mars, which recorded the January 6 event (Posner 2014, priv. comm.) as well, the event would be counted as a ground-level enhancement, GLE 72. However, on Earth there is a network of neutron monitors, and therefore an SEP event is only called a GLE if more than one station records a significant count rate increase. In contrast to EPHIN, all neutron monitors measure a particle distribution that is altered by the terrestrial magnetic field and its atmosphere, leading to daily and seasonal variation, but also to short-term changes due to the terrestrial magnetic field and the atmospheric shielding that depends on different factors such as the atmospheric pressure.

However, knowing the interplanetary magnetic field direction at Earth and using the EPHIN spectrum in forward-modeling as done in Matthiä et al. (2009) would allow

calculating the count rate increase not only for each neutron monitor, but also for other locations, allowing a more detailed investigation and more precise definition of GLEs.

Acknowledgements. The SOHO/EPHIN project is supported under Grant 50 OC 1302 by the German Bundesministerium für Wirtschaft through the Deutsches Zentrum für Luft- und Raumfahrt (DLR). We acknowledge the NMDB database (www.nmdb.eu) founded under the European Union's FP7 programme (contract No. 213007), and the PIs of individual neutron monitors for providing data. Furthermore, we would like to thank Galina Bazilevskaya for providing the PAMELA spectrum for the event in May 2012, and the ACE EPAM instrument team and the ACE Science Center for providing the ACE data. R.G.H. acknowledges the financial support of the Spanish Ministerio de Ciencia e Innovacion under project AYA2012-39810-C02-01.

References

- Band, D., Matteson, J., Ford, L., et al. 1993, *ApJ*, 413, 281
 Bazilevskaya, G. A., Mayorov, A. G., & Mikhailov, V. V. 2013, 33rd ICRC Proc.
 Böhm, E., Kharytonov, A., & Wimmer-Schweingruber, R. F. 2007, *A&A*, 473, 673
 Forbush, S. E. 1946, *Phys. Rev.*, 70, 771
 GEANT4 Collaboration 2006, CERN-LHCC 98-44, see also: <http://geant4.cern.ch/>
 Gopalswamy, N., Xie, H., Akiyama, S., et al. 2013, *ApJ*, 765, L30
 Matthiä, D., Heber, B., Reitz, G., et al. 2009, *J. Geophys. Res.*, 114, 8104
 Mewaldt, R. A., Looper, M. D., Cohen, C. M. S., et al. 2012, *Space Sci. Rev.*, 171, 97
 Moses, D., Droege, W., Meyer, P., & Evenson, P. 1989, *ApJ*, 346, 523
 Müller-Mellin, R., Kunow, H., Fleißner, V., et al. 1995, *Sol. Phys.*, 162, 483
 Papaioannou, A., Souvatzoglou, G., Paschalis, P., Gerontidou, M., & Mavromichalaki, H. 2014, *Sol. Phys.*, 289, 423
 Picozza, P., Galper, A. M., Castellini, G., et al. 2007, *Astropart. Phys.*, 27, 296
 Posner, A., Guetersloh, S., Heber, B., & Rother, O. 2009, *Space Weather*, 7, 05001
 Reames, D. V. 2013, *Space Sci. Rev.*, 175, 53
 Shen, C., Li, G., Kong, X., et al. 2013, *ApJ*, 763, 114
 Thakur, N., Gopalswamy, N., Xie, H., et al. 2014, *ApJ*, 790, L13
 Torsti, J., Valtonen, E., Lumme, M., et al. 1995, *Sol. Phys.*, 162, 505
 Tylka, A. J., Cohen, C. M. S., Dietrich, W. F., et al. 2006, *ApJSS*, 164, 536
 Warmuth, A. 2007, in *The High Energy Solar Corona: Waves, Eruptions, Particles*, eds. K.-L. Klein, & A. MacKinnon (Berlin, Heidelberg: Springer), *Lect. Notes Phys.*, 725, 107